Rapid Communications

Preparation of $SrTiO_3$ bicrystal substrates with atomic-level controlled boundaries for Josephson junction fabrication

Cui Ding,[1] Guanming Gong,[1] Chong Liu,[1] Haohao Yang,[1] Wenfeng Dong,[1] Zhiyu Zhang,[1] Yuanzhao Li,[1] Lili Wang,[1,2,*] and Qi-Kun Xue[1,2,3,†]

[1]*State Key Laboratory of Low-Dimensional Quantum Physics, Department of Physics, Tsinghua University, Beijing 10008, China*

[2]*Frontier Science Center for Quantum Information, Beijing 100084, China*

[3]*Beijing Academy of Quantum Information Sciences, Beijing 100193, China*

(Received 13 February 2020; accepted 7 April 2020; published 4 May 2020)

Grain-boundary Josephson junctions formed by epitaxial growth of high-temperature (T_c) superconductor films on bicrystal substrates have been employed to determine the pairing symmetry of high-T_c superconductivity. Since high-T_c superconductivity predominately takes place within a single unit cell along the c axis and superconducting coherence length is typically in the nanometer scale, the microstructure of grain boundaries of the bicrystal substrates is crucial for fabricating junctions required for Josephson tunneling study. In this study, we develop a two-step method to prepare insulating $SrTiO_3(001)$ bicrystal substrates with atomically uniform and coalesced grain boundaries. Using *in situ* scanning tunneling microscopy, we demonstrate that FeSe films grown on such substrates exhibit single-facet grain boundaries, leading to ideal Josephson junctions for investigating the pairing symmetry of FeSe superconductors.

DOI: 10.1103/PhysRevMaterials.4.050401

Since the discovery of high critical temperature (T_c) superconductivity in cuprate [1], fabricating Josephson junctions has been an active direction in both fundamental research and applications. Grain-boundary (GB) Josephson junctions consisting of two high-T_c superconducting films with different orientations have been often employed [2,3] to build superconducting quantum interference devices and investigate the symmetry of order parameter in high-T_c superconductivity [4–9]. In this regard, growing high-T_c superconducting films on bicrystal substrates with desired misorientation angles is one of the most direct ways to prepare GB junctions [6,10,11]. While epitaxial high-T_c superconducting films usually follow the orientations of the underlying bicrystals, segmental facets form around GBs because of meandering growth [12–17]. More importantly, the general facet microstructure causes wrong alignment of superconducting planes across GBs and locally depresses the superconducting order parameter that controls the tunneling process. With the faceted GBs, tunneling experiments heretofore suggest admixed $d+s$ pairing state with varying admixtures [18,19], in spite of the commonly accepted d-pairing symmetry [5].

The meandering growth and faceting configuration depend on film deposition condition, and more predominantly, on the microstructure of substrate GBs. The fused boundaries of commercial $SrTiO_3$ bicrystal substrates inevitably exhibit subnanometer-deep and nanometer-wide voids that disperse along small angle ($<10°$) GBs and even trenches with varied interedge distances of tens of nanometers along large-angle ones [17,20,21]. The edges of voids and trenches act as preferential nucleation sites, which generate multiple growth fronts of epitaxial films in turn. With increasing coverage, the numerous growth fronts could interrupt or overlap each other, forming segmental facets meandering through GBs [13,14,17]. Lowering the film-deposition rate could reduce the magnitude of meandering [14] but cannot eliminate the meandering process. The length of segmental facets ranges from a few to hundreds of nanometers [12–17], 1 or 2 magnitudes larger than the coherence length of high-T_c superconductors [22]. Consequently, such extrinsic features could induce spatially varied critical currents and be mixed up with contribution from intrinsic ones [17,23–27]. Performing rigorous tests to solve the puzzle of admixed pairing symmetries requires fabrication of single-facet GBs on the micrometer scale. To achieve this goal, preparing high-quality bicrystal substrates with atomically uniform GBs is a prerequisite.

In this work, we develop a two-step method, i.e., high-temperature annealing in ultrahigh vacuum (UHV) for GBs coalescence and low-temperature annealing with ozone flow to compensate oxygen loss in $SrTiO_3$ bicrystal substrates. We obtain simultaneously coalesced GBs, regular steps, and atomically flat surfaces for bicrystals with various fusion angles. *In situ* scanning tunneling microscopy (STM) observations reveal that the substrates prepared by this method are ideal for growing single-facet FeSe GB Josephson junctions.

We choose nominally symmetric $2 \times 15°$ and $2 \times 5°$ [001] tilted $SrTiO_3$ bicrystals with joint (001) surfaces (Shinkosha, Japan). We conduct the two-step annealing of the $SrTiO_3$ bicrystal substrates as well as FeSe film deposition in an UHV chamber with a base pressure better than 1×10^{-10} mbar. We grow FeSe films by codepositing Fe (99.995%) and Se (99.9999%) with a flux ratio of $\sim$1:10 and a growth rate of

*liliwang@mail.tsinghua.edu.cn
†qkxue@mail.tsinghua.edu.cn

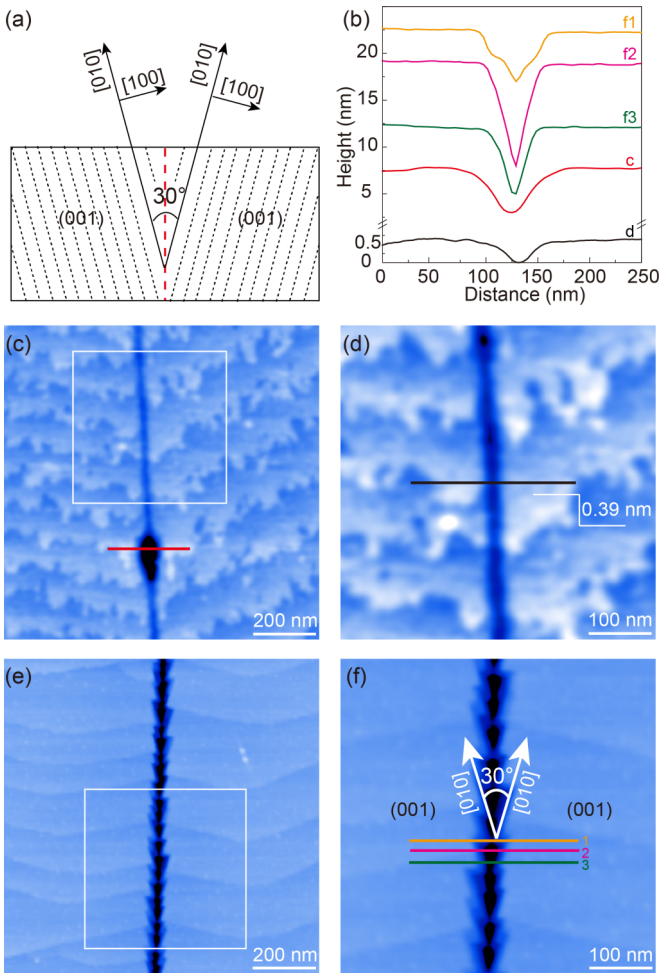

FIG. 1. Schematic and AFM morphologies of $SrTiO_3(001)$ bicrystal substrates. (a) Schematic of symmetric 2 × 15 ° [001] tilted $SrTiO_3(001)$ bicrystal substrates. (c)–(f) AFM topographic images of $SrTiO_3(001)$ bicrystal substrates as received [(c), (d)], and after the classical treatment in tube furnace [(e), (f)]. (d) and (f) are the zoom-in images corresponding to the areas marked by squares in (c) and (e), respectively. (b) Line profiles correspond to the colored lines in (c), (d), and (f).

0.1 unit cell (UC) per minute at 400 °C, similar to previous study [28]. We characterize the morphology and microscopic structure of GBs by both atomic force microscopy (AFM) and STM.

Figure 1(a) depicts a sketch of 2 × 15° [001] tilted $SrTiO_3$ bicrystal substrate, where the red dashed line marks the fusion boundary. Constant-force AFM topographic images of an as-received $SrTiO_3$ bicrystal substrate in Figs. 1(c) and 1(d) show similar morphology to other commercial ones [17,20,21]. The surface exhibits nearly straight fusion boundary and regularly distributed terraces with meandering steps of single-UC $SrTiO_3$ (0.39 nm) in height. The line profile crossing the border [the black curve in Fig. 1(b)] shows a depth of 0.6 nm and an edge-to-edge separation of ∼65 nm. A deep hollow with a diameter of 113 nm and a depth of 4.7 nm occasionally occurs along the boundary, as exemplified in Fig. 1(c) and the corresponding line profile [the red curve in Fig. 1(b)]. After traditional tube-furnace annealing under oxygen flux, the GB edges become saw-toothed, accompanied with formation of wide and deep trenches. Figures 1(e) and 1(f) display the typical GB morphologies of the bicrystal annealed at 1030 °C in a tube furnace under constant flow of high-purity oxygen, as previously reported for pristine single-crystal $SrTiO_3$ with regular stepped- and TiO_2-terminated surfaces [29]. After such annealing, significant straightening of atomic steps is evident indeed. However, the zigzag boundary is formed with many facets at both edges [labels in Fig. 1(f)]. Line profiles [the top three curves in Fig. 1(b)] show the trenches range from 10 to 85 nm in width, and 5 to 11 nm in depth. The average distance between two opposite edges is about 42 nm. The trenches with saw-toothed edges occur commonly in $SrTiO_3$ bicrystal substrates heated in air or under oxygen flux [20,21]. The trenches become more pronounced and more facets develop after prolonging annealing (not shown).

The GBs of this type lead to multiple faceted GBs in epitaxial FeSe films, which agree well with previous results in cuprate films [13–16]. Figures 2(a)–2(f) display the morphologies around the GBs with various coverages of FeSe from 1 to 30 UC on the same substrate, while Fig. 2(g) displays another with narrower trenches and 10-UC FeSe. The monolayer FeSe films follow the morphology of the substrate [Fig. 2(a)]. With increasing coverage, FeSe films on two grains gradually merge together [Figs. 2(c)–2(e), and 2(g)]. Most merged fronts exhibit height difference of 0.88–1.69 nm, as exemplified by the white lines in Figs. 2(d) and 2(g). Obviously, the situation gives rise to in-plane misalignment of most superconducting planes between two sides of the boundary; 5% of them are in-plane aligned [Fig. 2(e)] but the boundaries are atomically disordered. As demonstrated in the atomically resolved image and the corresponding fast Fourier transformation (FFT) image in Fig. 2(f), although the FeSe films follow the orientation of respective $SrTiO_3$ grains, the lattice around the merging region, in a range of 2 ∼ 3 nm, is significantly distorted, where the top-layer Se atoms exhibit higher contrast of 50–100 pm.

The formation of misaligned epitaxial GBs is due to the wide trenches with saw-toothed edges in substrates, which can be demonstrated by the schematic depicted in Fig. 2(h). Due to the two-dimensionality of the material, the growth fronts of FeSe films from two grains could overflow their respective edges, and meet and intersect firstly at the locations with narrower separation (left panel) and then at those with larger separation (right panel). Due to the wide range, from 10 to 85 nm, of interedge separation, the asynchronous merging induces complicated alignment and even spiral dislocations around GBs [Fig. 2(g)].

We could obtain nearly ideally coalesced GBs on insulating $SrTiO_3$ bicrystals by using the two-step method, as displayed in Fig. 3. Here, we use SiC substrates as heating source. As illustrated in Fig. 3(a), when either direct current (DC) or alternating current (AC) flows through the SiC substrate, the upper $SrTiO_3$ bicrystals get heated indirectly. Figure 3(b) depicts the detailed processes of two-step annealing. The first-step UHV annealing includes degassing at 650 °C for 30 min and sequential annealing at 950 °C for 1 hour and 1000 °C for 20 min while the pressure is kept better than 1×10^{-9} mbar (the three blue frames). The $SrTiO_3$ substrates gradually get dark with oxygen desorption during UHV annealing, and

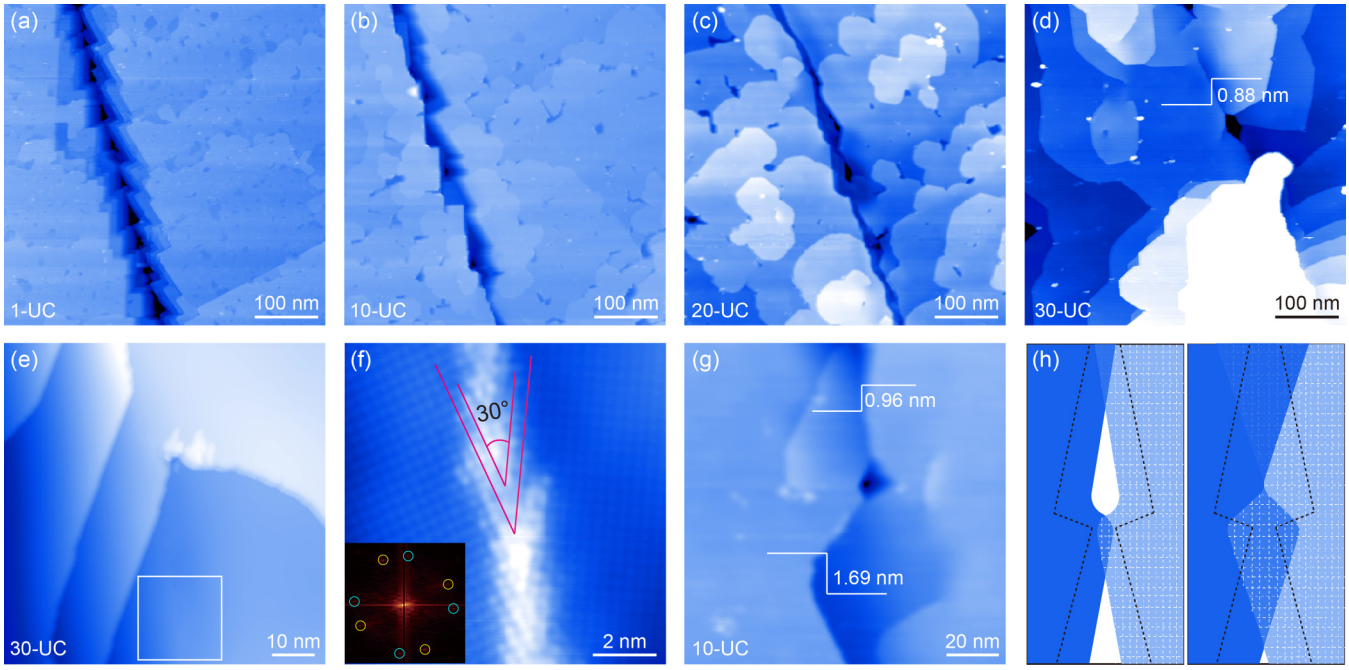

FIG. 2. STM topographic images of FeSe films GBs on the saw-toothed $SrTiO_3$(001) bicrystal substrates. (a)–(f) STM topographic images after 1-UC (a), 10-UC (b), 20-UC (c), and 30-UC (d)–(f) FeSe films are deposited sequentially on the same substrates, while (g) 10-UC FeSe on another bicrystal substrate with narrower boundary trenches. (a)–(d), (g): sample bias $V_s = 2 - 3$ V, tunneling current $I = 50 - 100$ pA. (e) and (f) are taken at 4.8 K, (e) $V_s = 2$ V, $I = 20$ pA and (f) $V_s = 150$ mV, $I = 200$ pA. (f) Zoom-in image corresponding to the area marked by square in (e). The inset in (f) is the corresponding FFT image with the yellow and light blue circles marking the 1×1 Bragg points with a relative rotation angle of 30°. (h) Schematic showing the morphology evolution around GBs from low coverage (left panel) to high coverage (right panel). The dashed lines symbolize boundary edges of $SrTiO_3$ bicrystal, and the blue solid and white dashed patterns represent the films epitaxial from the left and right grains, respectively.

spatial gradient of oxygen vacancy content occurs under DC heating [see the top two sample photos in Fig. 3(b)], due to surface stoichiometry polarization effect [30]. In contrast, the spatial distribution of oxygen vacancies gets uniform under AC heating [see the bottom sample photo in Fig. 3(b)].

Now we move to the surface morphology evolution during UHV annealing. Figures 3(c)–3(e) display morphologies under DC heating, as labeled correspondingly in Fig. 3(b). The trenches of the substrate after degassing are ∼18 nm wide and 0.8 nm (equal to 2-UC $SrTiO_3$) deep, as shown in Fig. 3(c) and by the corresponding line profile in Fig. 3(g). After annealing in UHV at 950 °C, saw-toothed edges [Fig. 3(d)] form as a result of atom migration, but the trench depth remains at 2 UC and the width reduces to 4–18 nm [the line profile labeled with d in Fig. 3(g)]. After annealing at 1000 °C, 57% of GBs are coalesced, while regular surface with straight steps of single-UC $SrTiO_3$ and atomically flat terraces form in each grain, as displayed in Fig. 3(e). The remaining voids are 1-UC deep and 5–6 nm wide [the line profile labeled with e in Fig. 3(g)]. The coalesce ratio is further increased under AC heating. As demonstrated in the mosaic STM image in Fig. 3(h), the coalescence ratio increases to 78% and the voids are only 2–4 nm wide. Notably, we occasionally observe terrace mismatch points accompanied with voids, as indicated by the yellow arrow in Fig. 3(f), which could not coalesce completely due to the spiral step of 1-UC $SrTiO_3$.

The UHV annealing creates oxygen vacancies and converts the $SrTiO_3$ to the metallic state, which will be an issue for transport measurements. On the other hand, it is imperative to take appropriate annealing under ozone flux to finely tune the surface oxygen content, an essential factor that determines the properties of $SrTiO_3$ and its interface coupling with upper epitaxial films [31–33]. We carry out the second-step annealing at relative low temperatures of 680–760 °C in an ozone pressure of 1.9×10^{-5} mbar [the purple chart in Fig. 3(b)] to replenish oxygen while keeping the GB coalesced. After that, the $SrTiO_3$ bicrystal substrates recover their initial insulating state. Thus, STM characterization is achievable only after deposition of metallic FeSe films.

Figure 4 displays the STM images of ultrathin FeSe films on the bicrystal $SrTiO_3$ substrates treated by the two-step method. GBs free of meandering form in both monolayer [Fig. 4(a)] and multilayer FeSe films [Fig. 4(e)]. In Fig. 4(a), the monolayer FeSe films cover 57% of the GB, while the voids along the boundary have a consistent depth of 0.55 nm (equal to 1-UC FeSe), the same as the one in grain interiors (scattered dark areas). With the coverage of FeSe increasing to above 1 UC, homogeneous GBs form. As demonstrated in Fig. 4(e), the single-facet FeSe film GB with exact plane-to-plane alignment extends in the whole scanning range of 1.1 μm, even at a terrace mismatch point (marked by the yellow arrow).

Meanwhile, the GBs become more uniform and atomically ordered. Figures 4(b) and 4(c) display the atomically resolved STM images for monolayer and 5-UC FeSe grown on 2×15 ° tilted $SrTiO_3$ bicrystal, respectively, while Fig. 4(d)

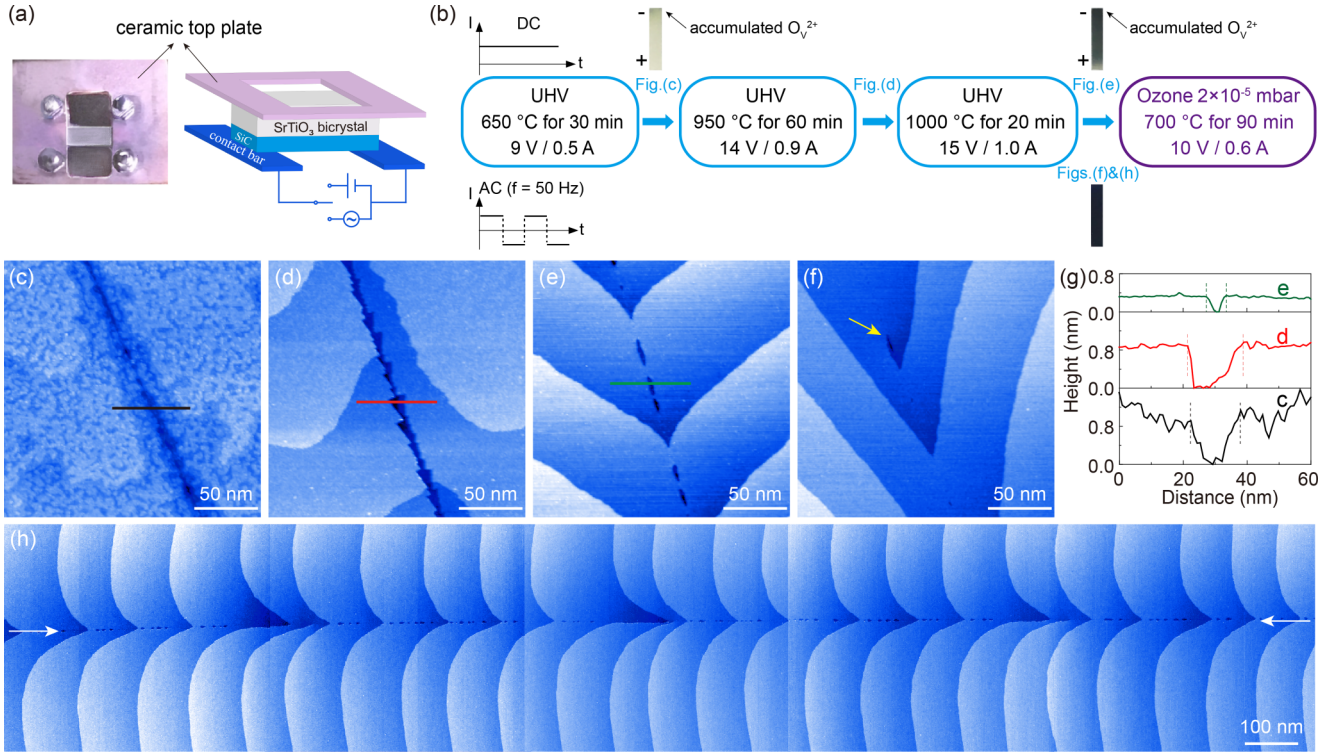

FIG. 3. Schematic illustration of heating setup (a), annealing flow chart (b), and the evolution of GBs in $SrTiO_3$(001) bicrystal substrates with UHV annealing (c)–(h). The STM topographic images ($V_s = 2$ V, $I = 50$ pA) after sequential annealing under DC heating (c)–(e) and under AC heating (f) and (h) are labeled with the corresponding steps in (b). (g) Line profiles correspond to the colored lines in (c)–(e). The yellow arrow in (f) marks the terrace mismatch point, and the white arrows in (h) mark the GB.

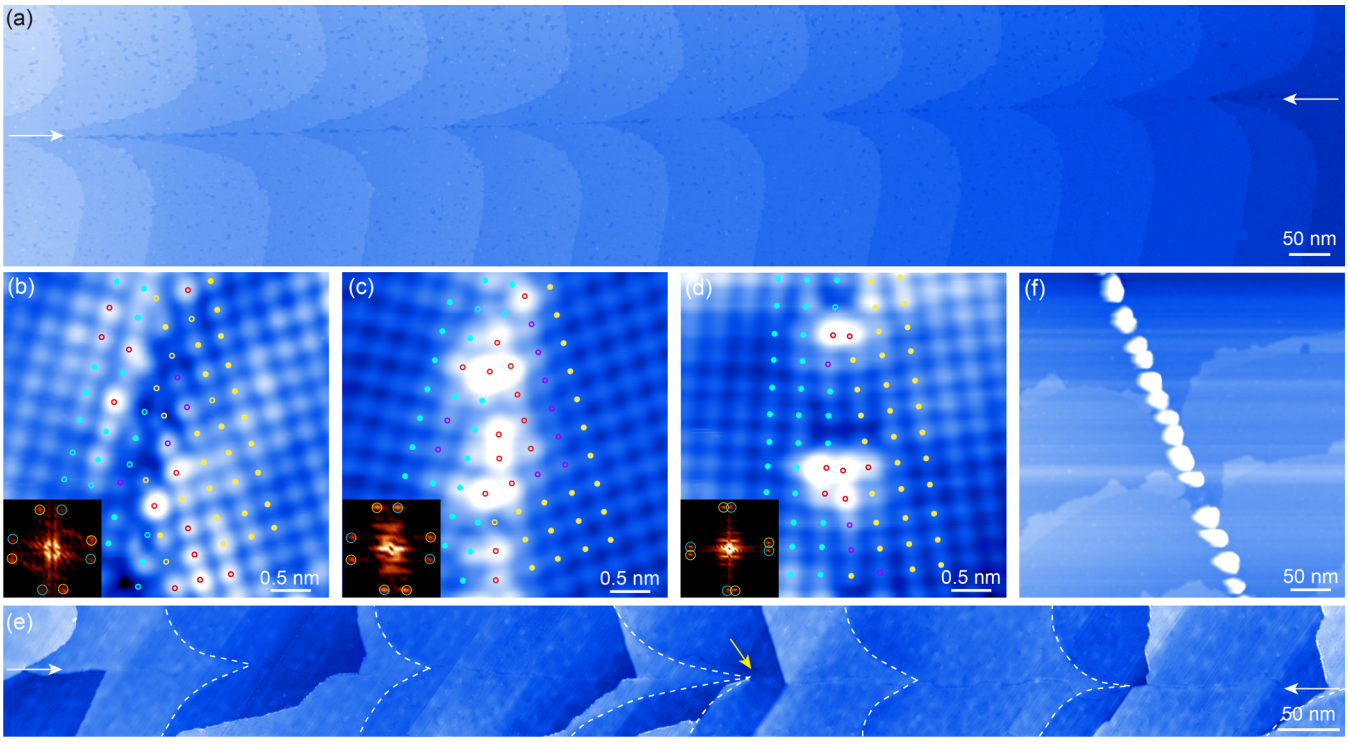

FIG. 4. STM topographic morphologies of FeSe film GBs on two-step annealed $SrTiO_3$(001) bicrystal substrates with AC heating. (a), (b), (f) for ~1-UC FeSe, (c) for 5-UC FeSe, (d) for 3-UC FeSe, and (e) for 6-UC FeSe films. (a)–(d) are taken at 77 K, (a) $V_s = 1$ V, $I = 50$ pA and (b)–(d) $V_s = 120$ mV, $I = 100$ pA. (e) and (f) $V_s = 9.5$ V, $I = 50$ pA. The white arrows in (a) and (e) mark the GBs, the yellow arrow in (e) marks the terrace mismatch point, and the dashed lines in (e) mark the steps of $SrTiO_3$ substrates. In (b)–(d), the blue and yellow dots mark the Se atoms at regular lattices in the respective right and left domains, while the colored circles around GBs mark the Se atoms either that occupy the regular latices but appear darker (blue and yellow) or brighter (red), or that displaced from the rectangular structure (magenta).

shows the images for 3-UC FeSe on the 2 × 5 ° one. The epitaxial FeSe follows the orientation of substrates in each grain, as marked by blue and yellow dots for left and right grains, respectively. The corresponding FFTs clearly show two sets of lattices with a misorientation angle of 30° and 10°, consistent with those of bicrystal substrates. Due to intrinsic strain at boundaries, some dislocations occur where some Se atoms show apparent contrast [see the circles marked in Figs. 4(b)–4(d)]. Regardless of these features, the overall microstructure of the GBs is significantly improved compared to that on the grooved GBs [Fig. 2(f)], with nearly perfect atomic structure on both sides of the boundary.

In contrast to the boundaries with saw-toothed edges, the coalesced GBs favor uniform nucleation and continuous flow growth. Consequently, the GBs of the FeSe films with exact in-plane alignment form right along the coalesced GBs in bicrystal substrates. Under the current growth condition, the epitaxial FeSe films can flow over voids with width <4 nm, usually in company with a total coalescence ratio >75%, to form uniform GBs. Along the boundaries with lower coalescence ratio, FeSe clusters could form instead. Figure 4(f) displays the morphology of FeSe films on a bicrystal substrate with a lower coalescence ratio of 68% wherein the residual voids have a larger maximum width of 5 nm. The 1-UC FeSe films cover each grain uniformly, whereas some isolated FeSe islands of ∼6 nm high reside along GBs, resulted from preferential nucleation at void edges. This again indicates that the coalesced GBs is prerequisite for obtaining in-plane aligned GBs of epitaxial films.

In summary, we develop a two-step method to prepare high-quality insulating bicrystal $SrTiO_3$ substrates with coalesced GBs, regular steps, and atomically flat surface. The method is controllable and reproducible for $SrTiO_3$ bicrystals with various misorientation angles (at least up to 2 × 22.5° as we have tried). We demonstrate the applicability of the $SrTiO_3$ bicrystals to fabricating single-facet epitaxial film GBs with exact in-plane alignment in ultrathin films of FeSe. Obviously, the resulting superconducting film GB junctions form an ideal platform for investigating the intrinsic properties of Josephson junctions and the pairing symmetry of high-T_c superconductors. At last, we point out that the two-step annealing is a flexible treatment, for the GB coalesce and oxygen replenishment are accomplished separately and independently. The $SrTiO_3$ bicrystals treated with the flexible two-step annealing can act as ideal substrates for other oxide heterostructures to explore novel properties and promote performance.

This work is supported by the National Natural Science Foundation of China (Grants No. 11774193 and No. 11790311) and the National Basic Research Program of China (Grant No. 2017YFA0303303).

[1] J. G. Bednorz and K. A. Müller, Possible high T_c superconductivity in the Ba-La-Cu-O system, Z. Phys. B **64**, 189 (1986).

[2] P. Chaudhari, J. Mannhart, D. Dimos, C. C. Tsuei, J. Chi, M. M. Oprysko, and M. Scheuermann, Direct Measurement of the Superconducting Properties of Single Grain Boundaries in $YBa_2Cu_3O_{7-\delta}$, Phys. Rev. Lett. **60**, 1653 (1988).

[3] D. Dimos, P. Chaudhari, J. Mannhart, and F. K. LeGoues, Orientation Dependence of Grain-Boundary Critical Currents in $YBa_2Cu_3O_{7-\delta}$ Bicrystals, Phys. Rev. Lett. **61**, 219 (1988).

[4] C. C. Tsuei, J. R. Kirtley, C. C. Chi, Y.-J. Lock See, A. Gupta, T. Shaw, J. Z. Sun, and M. B. Ketchen, Pairing Symmetry and Flux Quantization in a Tricrystal Superconducting Ring of $YBa_2Cu_3O_{7-\delta}$, Phys. Rev. Lett. **73**, 593 (1994).

[5] C. C. Tsuei and J. R. Kirtley, Pairing symmetry in cuprate superconductors, Rev. Mod. Phys. **72**, 969 (2000).

[6] H. Hilgenkamp and J. Mannhart, Grain boundaries in high-T_c superconductors, Rev. Mod. Phys. **74**, 485 (2002).

[7] F. Tafuri and J. R. Kirtley, Weak links in high critical temperature superconductors, Rep. Prog. Phys. **68**, 2573 (2005).

[8] A. I. Akimenko, F. Bobba, F. Giubileo, V. A. Gudimenko, S. Piano, and A. M. Cucolo, Evidence of a *s*-wave subdominant order parameter in $YBa_2Cu_3O_{7-\delta}$ from break-junction tunneling spectra, Low Temp. Phys. **36**, 167 (2010).

[9] P. Seidel, Josephson effects in iron based superconductors, Supercond. Sci. Technol. **24**, 043001 (2011).

[10] K. Char, M. S. Colclough, S. M. Garrison, N. Newman, and G. Zaharchuk, Bi-epitaxial grain boundary junctions in $YBa_2Cu_3O_7$, Appl. Phys. Lett. **59**, 733 (1991).

[11] K. Char, M. S. Colclough, L. P. Lee, and G. Zaharchuk, Extension of the bi-epitaxial Josephson junction process to various substrates, Appl. Phys. Lett. **59**, 2177 (1991).

[12] J. A. Alarco, E. Olsson, Z. G. Ivanov, N. P., D. Winkler, E. A. Stepantsov, and A. Y. Tzalenchuk, Microstructure of an artificial grain boundary weak link, Ultramicroscopy **51**, 239 (1993).

[13] C. Træholt, J. G. Wen, H. W. Zandbergen, Y. Shen, and J. W. M. Hilgenkamp, TEM investigation of $YBa_2Cu_3O_7$ thin films on $SrTiO_3$ bicrystals, Physica C **230**, 425 (1994).

[14] X. F. Zhang, D. J. Miller, and J. Talvacchio, Control of meandering grain boundary configurations in $YBa_2Cu_3O_y$ bicrystal thin films based on deposition rate, J. Mater. Res. **11**, 2440 (1996).

[15] X.-F. Zhang, V. R. Todt, and D. J. Miller, From meandering to straight grain boundaries: Improving the structures of artificially induced grain boundaries in superconducting $YBa_2Cu_3O_y$ bicrystals, J. Mater. Res. **12**, 3029 (1997).

[16] J. G. Wen, T. Takagi, and N. Koshizuka, Microstructural studies on YBCO film bicrystals with large single facet grain boundaries grown by liquid phase epitaxy, Supercond. Sci. Technol. **13**, 820 (2000).

[17] H.-W. Yu, M.-J. Chen, H. C. Yang, S. Y. Yang, and H. E. Horng, Effect of the grooved $SrTiO_3$ bicrystal line on the $YBa_2Cu_3O_7$ grain boundary, Physica C **333**, 163 (2000).

[18] Q. Li, Y. N. Tsay, M. Suenaga, R. A. Klemm, G. D. Gu, and N. Koshizuka, BiSrCaCuO Bicrystal *c*-Axis Twist Josephson Junctions: A New Phase-Sensitive Test of Order Parameter Symmetry, Phys. Rev. Lett. **83**, 4160 (1999).

[19] H. J. Smilde, A. A. Golubov, Ariando, G. Rijnders, J. M. Dekkers, S. Harkema, D. H. Blank, H. Rogalla, and H. Hilgenkamp, Admixtures to *d*-Wave Gap Symmetry in Untwinned $YBa_2Cu_3O_7$ Superconducting Films Measured by Angle-Resolved Electron Tunneling, Phys. Rev. Lett. **95**, 257001 (2005).

[20] Q. D. Jiang, X. Q. Pan, and J. Zegenhagen, Atomic-scale structure of a $SrTiO_3$ bicrystal boundary studied by scanning tunneling microscopy, Phys. Rev. B **56**, 6947 (1997).

[21] Q. D. Jiang, Z. J. Huang, A. Brazdeikis, M. Dezaneti, C. L. Chen, P. Jin, and C. W. Chu, Nondestructive investigation of microstructures and defects at a $SrTiO_3$ bicrystal boundary, Appl. Phys. Lett. **72**, 3365 (1998).

[22] C. W. Chu, L. Z. Deng, and B. Lv, Hole-doped cuprate high temperature superconductors, Physica C **514**, 290 (2015).

[23] H. Hilgenkamp, J. Mannhart, and B. Mayer, Implications of $d_{x^2-y^2}$ symmetry and faceting for the transport properties of grain boundaries in high T_c superconductors, Phys. Rev. B **53**, 14586 (1996).

[24] L. Alff, S. Kleefisch, U. Schoop, M. Zittartz, T. Kemen, T. Bauch, A. Marx, and R. Gross, Andreev bound states in high temperature superconductors, Eur. Phys. J. B **5**, 423 (1998).

[25] M. Carmody, K. L. Merkle, Y. Huang, L. D. Marks, and B. H. Moeckly, The relation between barrier structure and current uniformity in YBCO Josephson junctions, Interface Sci. **8**, 231 (2000).

[26] F. Sandiumenge, N. Vilalta, J. Rabier, and X. Obradors, Subgrain boundary structure in melt-textured $RBa_2Cu_3O_7$ (R = Y, Nd): Limitation of critical currents versus flux pinning, Phys. Rev. B **64**, 184515 (2001).

[27] D. M. Feldmann, T. G. Holesinger, R. Feenstra, and D. C. Larbalestier, A review of the influence of grain boundary geometry on the electromagnetic properties of polycrystalline $YBa_2Cu_3O_{7-x}$ films, J. Am. Ceram. Soc. **91**, 1869 (2008).

[28] W.-H. Zhang, Y. Sun, J.-S. Zhang, F.-S. Li, M.-H. Guo, Y.-F. Zhao, H.-M. Zhang, J.-P. Peng, Y. Xing, H.-C. Wang, T. Fujita, A. Hirata, Z. Li, H. Ding, C.-J. Tang, M. Wang, Q.-Y. Wang, K. He, S.-H. Ji, X. Chen, J.-F. Wang, Z.-C. Xia, L. Li, Y.-Y. Wang, J. Wang, L. Wang, M.-W. Chen, Q.-K. Xue, and X.-C. Ma, Direct observation of high-temperature superconductivity in one-unit-cell FeSe films, Chin. Phys. Lett. **31**, 017401 (2014).

[29] N. Erdman, K. R. Poeppelmeier, M. Asta, O. Warschkow, D. E. Ellis, and L. D. Marks, The structure and chemistry of the TiO_2-rich surface of $SrTiO_3$ (001), Nature (London) **419**, 55 (2002).

[30] C. Rodenbucher, P. Meuffels, G. Bihlmayer, W. Speier, H. Du, A. Schwedt, U. Breuer, C. L. Jia, J. Mayer, R. Waser, and K. Szot, Electrically controlled transformation of memristive titanates into mesoporous titanium oxides via incongruent sublimation, Sci. Rep. **8**, 3774 (2018).

[31] C. Chen, J. Avila, E. Frantzeskakis, A. Levy, and M. C. Asensio, Observation of a two-dimensional liquid of Fröhlich polarons at the bare $SrTiO_3$ surface, Nat. Commun. **6**, 8585 (2015).

[32] Z. Wang, S. M. Walker, A. Tamai, Y. Wang, Z. Ristic, F. Y. Bruno, A. de la Torre, S. Riccò, N. C. Plumb, M. Shi, P. Hlawenka, J. S. Barriga, A. Varykhalov, T. K. Kim, M. Hoesch, P. D. C. King, W. Meevasana, U. Diebold, J. Mesot, B. Moritz, T. P. Devereaux, M. Radovic, and F. Baumberger, Tailoring the nature and strength of electron–phonon interactions in the $SrTiO_3$(001) 2D electron liquid, Nat. Mater. **15**, 835 (2016).

[33] G. M. Gong, H. Yang, Q. H. Zhang, C. Ding, J. S. Zhou, Y. J. Chen, F. Q. Meng, Z. Y. Zhang, W. F. Dong, F. W. Zheng, P. Zhang, L. X. Yang, L. Gu, Q.-K. Xue, and L. Wang, Oxygen vacancy modulated superconductivity in monolayer FeSe on $SrTiO_{3-\delta}$, Phys. Rev. B **100**, 224504 (2019).